Nanoelectronics and Its New Materials – A NEW ERA OF NANOSCIENCE

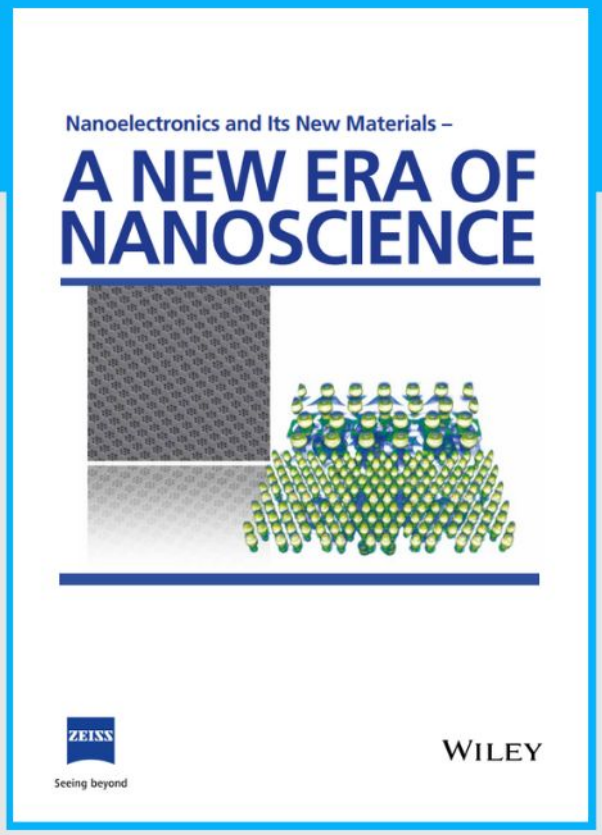

Discover the recent advances in electronics research and fundamental nanoscience.

Nanotechnology has become the driving force behind breakthroughs in engineering, materials science, physics, chemistry, and biological sciences. In this compendium, we delve into a wide range of novel applications that highlight recent advances in electronics research and fundamental nanoscience. From surface analysis and defect detection to tailored optical functionality and transparent nanowire electrodes, this eBook covers key topics that will revolutionize the future of electronics.

To get your hands on this valuable resource and unleash the power of nanotechnology, simply download the eBook now. Stay ahead of the curve and embrace the future of electronics with nanoscience as your guide.

ZEISS

Seeing beyond

WILEY

ADVANCED FUNCTIONAL MATERIALS
www.afm-journal.de

Frequency Modulation Based Long-Wave Infrared Detection and Imaging at Room Temperature

*Tianyi Guo, Arindam Dasgupta, Sayan Chandra, Swastik Ballav, Pablo Cencillo-Abad, Souptik Mukherjee, Aritra Biswas, Muhammad Waqas Shabbir, and Debashis Chanda**

Detection of long wave infrared (LWIR) light at room temperature is a long-standing challenge due to the low energy of photons. A low-cost, high-performance LWIR detector or camera that operates under such conditions is pursued for decades. Currently, all available detectors operate based on amplitude modulation (AM) and are limited in performance by AM noises, including Johnson noise, shot noise, and background fluctuation noise. To address this challenge, a frequency modulation (FM)-based detection technique is introduced, which offers inherent robustness against different types of AM noises. The FM-based approach yields an outstanding room temperature noise equivalent power (NEP), response time, and detectivity (D*). This result promises a novel uncooled LWIR detection scheme that is highly sensitive, low-cost, and can be easily integrated with electronic readout circuitry, without the need for complex hybridization.

1. Introduction

Long-wave infrared (LWIR) detectors are integral components in various applications like night vision, chemical sensing, spectroscopy, industrial inspection, space exploration, medical imaging, food evaluation technologies, security surveillance, firefighting, and defense-rated applications.[1–3] The currently available LWIR detectors can be broadly categorized into two types: cooled and uncooled detectors with both having their own limitations. Cooled detectors, predominantly fabricated using Mercury-Cadmium-Telluride (MCT), exhibit excellent detectivity ranging from 10^9 to 10^{11} Jones. However, the requirement of cryogenic cooling makes them expensive and limits their practical utility.[4–6] On the other hand, uncooled detectors such as microbolometers can operate at room temperature and are relatively cost-effective. But, microbolometers suffer from low detectivity ($\approx 10^8$ Jones) due to the higher thermal noise level intrinsic to room temperature operation and slow response time (15–20 ms).[4,7,8] Concomitantly, all present cooled as well as uncooled detectors employ amplitude modulation (AM) detection of photocurrent, voltage, or resistance changes in response to light exposure. All of these AM-based detection techniques inherently suffer from Johnson noise, thermal noise, and shot noises which are all AM noises.[9,10] Therefore, there is an immense need for an uncooled LWIR detector that offers high detectivity and better signal-to-noise response.

Here, we propose a frequency modulation (FM)-based LWIR detection scheme based on an oscillating circuit using a phase-change material. While the operation of the microbolometer relies on the change in resistance based on small disturbance to the material properties with a positive resistance characteristic, the proposed scheme operates through FM of the circuit, achieved by utilizing the Negative Differential Resistance (NDR) of the phase change material(PCM) where the film experiences drastic phase changes between insulating and metallic phases. This FM-based detection mechanism provides inherent resilience against noise, particularly noise of AM nature. In this work, VO_2 is selected as the PCM. At room temperature, VO_2 is in its insulating phase possessing a monoclinic crystal structure with high resistance.[11–13] However, when subjected to elevated thermal conditions, VO_2 undergoes an insulator-to-metal transition (IMT) to a rutile structure known as the metallic phase, displaying orders of magnitude lower resistance.[14,15] With the reversal of the thermal condition, the transition is reversible from the metallic phase to the insulating phase (MIT).[16,17] This thermally induced transition in VO_2 is exceptionally robust compared to other PCM and with a low thermal hysteresis (5–8 K).[18,19] In the phase transition range, VO_2 exhibits a NDR behavior,[20] where the differential resistance $\Delta V/\Delta I < 0$. A combination of an NDR element with a capacitor creates an electrical oscillator circuit that can self-sustain current/voltage oscillation without the need for an external inductive component.[21–25] In the case of VO_2, repeated oscillation between the two phases occurs, with the IMT and the MIT following each other. To enhance the

T. Guo, S. Ballav, D. Chanda
Department of Physics
University of Central Florida
Orlando, FL 32816, USA
E-mail: debashis.chanda@ucf.edu
T. Guo, A. Dasgupta, S. Chandra, S. Ballav, P. Cencillo-Abad, S. Mukherjee, A. Biswas, M. W. Shabbir, D. Chanda
NanoScience Technology Center
University of Central Florida
Orlando, FL 32826, USA
A. Biswas, D. Chanda
CREOL
University of Central Florida
Orlando, FL 32816, USA
The ORCID identification number(s) for the author(s) of this article can be found under https://doi.org/10.1002/adfm.202309298

DOI: 10.1002/adfm.202309298

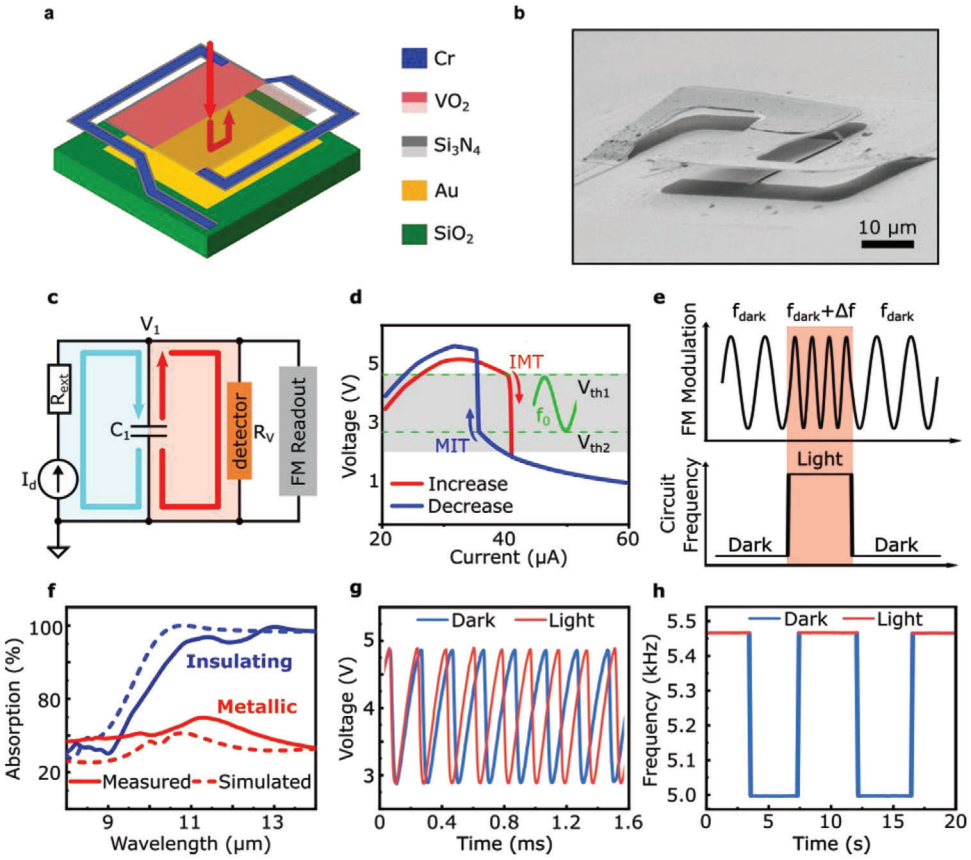

Figure 1. FM based infrared detection. a) Schematic illustration and b) corresponding scanning electron microscope (SEM) image of the device. c) Circuit diagram of the FM measurement setup. d) Current-vs-voltage plot of the device with an external resistor of 58 kΩ. e) Schematic illustration of the FM detection scheme. f) Measured and simulated absorption spectra of the detector in the wavelength range of 8 to 14 μm in insulating (Blue) and metallic (Red) phase. g) Oscillation waveforms during the dark (Blue) and light (Red) conditions. A higher oscillation frequency is observed when the detector is illuminated with light and the corresponding shift in the oscillation frequency is shown in h).

optical absorption and sensitivity of the detector, the VO_2 thin film is placed on an optical cavity. The FM-based LWIR detection is achieved by tracking the change in oscillator frequency of the circuit with respect to the incident power, while the VO_2 film is electrically biased in the high-temperature coefficient of resistance (TCR) at the IMT transition edge. While a LWIR detector utilizing the NDR of PCM in conjunction with FM-based detection has yet to be reported, prior research has demonstrated the successful creation of self-oscillators with NDR using various PCM, such as metal oxides and 2D materials.[26–29] Consequently, for the purpose of presenting a general detection scheme, we use the terms PCM and VO_2 interchangeably in the following description. Our room-temperature LWIR detector exhibits a noise equivalent power (NEP) of less than 3 pW · $Hz^{-1/2}$, response time ≈2.96 ms and a high detectivity of the order of 10^9 comparable to cryogenically cooled LWIR detectors. We strongly believe that the performance can be further enhanced with proper industry-scale packaging. This novel concept provides a paradigm shift to highly sensitive, uncooled LWIR detectors that can be used in IR spectrometers for molecular sensing, medical diagnostics, and cameras for space, military, and security applications.

2. Results

2.1. Device Principle

The schematic design of the FM-based LWIR detector is shown in **Figure 1**a. A thin PCM film is suspended with a Si_3N_4 support layer on top of an air spacer and an Au mirror. The Au mirror and air spacer together form an optical cavity. A part of the PCM/Si_3N_4 stack in the schematic is intentionally drawn with transparency to clearly show the presence of the optical cavity. The incident infrared radiation (indicated by the red arrow) is partially absorbed and partially transmitted through the thin film stack. The transmitted wave is then reflected by the back mirror. Depending on the cavity phase, a constructive interference between the reflected wave and incident wave intensifies the electromagnetic field at the suspended PCM/Si_3N_4 stack interface resulting in an enhancement in absorption.[30] Finally, chromium electrodes were fabricated on the sides of the PCM for electrical connections.

A Scanning Electron Microscope (SEM) image of the detector is shown in Figure 1b, where a suspended 8 × 8 μm^2 PCM/Si_3N_4 stack is clearly visible. Details of the device fabrication are

included in the Experimental section. The fabricated detector pixel is connected to an electrical circuit as illustrated in Figure 1c. At an appropriate biasing condition, electrical oscillations can be initiated owing to the NDR exhibited by the PCM in the active pixel material stack. The onset of oscillation under current control (CC)[31] mode is depicted in Figure 1c. The two halves in the circuit diagram, highlighted by blue and red colors, represent two processes in the oscillation. The blue process indicates the charging of capacitor C_1 when the circuit is first initiated. During this process, the current flow I_d bypasses the active detector pixel (R_v) branch due to its high resistance in the insulating phase of PCM, instead charges the capacitor C_1. Following the charging of C_1 (shaded as the blue process in Figure 1c), the discharging of C_1 (shaded as the red process in Figure 1c) starts as soon as the voltage V_1 across C_1 exceeds a certain threshold to drive sufficient current through R_v to induce an IMT due to the increase in local Joule heating.[32–34] After the IMT, the PCM (R_v) transits to a metallic phase with considerably lower resistance compared to its insulating phase, resulting in the discharging of capacitor C_1. Subsequently, the voltage across C_1 (V_1) decreases, eventually leading to an MIT in the PCM due to the significant decrease in the current/Joule heating.

The continuous repetition of these two processes results in the oscillation in current/voltage across the PCM. One complete electrical oscillation cycle includes one rise and one fall of the voltage V_1 across the PCM (R_v). The rise and fall time can be understood as the time required to travel between two threshold voltages V_{th1} and V_{th2}, where V_{th1} is the threshold voltage at the end of the C_1 charging ($V_1 > V_{th1}$) when the IMT occurs, and V_{th2} is the threshold voltage at the end of C_1 discharging ($V_1 < V_{th2}$) when the MIT happens. To acquire the full hysteresis curve of the VO_2 phase transition, we measure the change in the voltage across the VO_2 film by varying the bias current. An external resistor $R_{ext} = 58\ k\Omega$ is added to the circuit (Figure 1c) to disable electrical oscillation while varying the applied current. Figure 1d plots the measured voltage across the PCM as a function of the bias current. The sudden drop in the voltage in the red curve while increasing the applied current represents IMT; whereas the sudden bump in the voltage while decreasing the applied current represents MIT. The voltages across the PCM (V_1) at the transition edges are recorded as the threshold voltages V_{th1} and V_{th2}, respectively. During the LWIR exposure of the device, the stack absorbs the light and modifies the phase of PCM toward metallic phase. Although, this modification is not strong enough to induce the phase transition due to the low intensity of the incident light, it reduces both threshold voltages V_{th1} near IMT and V_{th2} near MIT resulting in the shift in the oscillation frequency. Figure 1e shows a schematic illustration of the working principle of this proposed FM-based detection scheme. At first, during dark conditions, the circuit oscillates at a frequency of $f_{dark.}$ When the detector is illuminated with infrared light, it changes the oscillation frequency to $f_{dark}+\Delta f$. Once the incident light is removed, the oscillation frequency returns to its original frequency. Therefore, by recording the frequency shift Δf, the incoming infrared light can be detected.

The absorption spectra of the PCM/Si_3N_4 stack in the insulating (blue) and metallic (red) phases are measured and plotted in Figure 1f where a significant change in absorption between the two end states is observed. To corroborate the experimental data with numerical calculations, we perform finite difference time domain (FDTD) simulations in Ansys Lumericals, where there is a good agreement between the simulation (dashed) and experimental results (solid) (see Experimental section for the details of the FDTD simulation). We consider the absorption of the stack during oscillation to be in between the metallic and insulating phase absorptions. Figure 1g shows two measured electrical oscillation waveforms in dark (blue) and light (red) conditions, with the time between the two waveforms adjusted to best present the difference in oscillation frequency. The corresponding oscillation frequencies in the light (red) and dark (blue) conditions are displayed in Figure 1h. For the light illumination, a quantum cascade laser (QCL) of wavelength 8.7 μm is focused on the detector using a parabolic mirror. When the $8 \times 8\ \mu m^2$ active sensing area with a current of 63 μA is illuminated with a 11.5 μW incident power with 300 μm diameter spot size, the oscillation frequency increases by 499 Hz, from 5.007 kHz (dark) to 5.506 kHz (light). A schematic of the measurement setup is shown in Figure S1 (Supporting Information), while the details of the setup are included in the Experimental Section.

2.2. Equivalent Circuit Model

While extensive research has been done on the phase transition of VO_2, the physics behind the phase transition when it is simultaneously driven by current and electric field (in this case incident infrared light), is not well understood. A good model that can describe the full transition is still being explored. For this reason, it is daunting to simulate the oscillation frequency and light-induced FM of our device at the same time for a wide range of currents, because this would require describing the phase transition both under DC (bias current) and high frequency (incident IR radiation) electric fields. We instead followed an approximate approach by creating an equivalent circuit of the device in a circuit simulation environment to match and predict the electrical performance of the device. To simulate the oscillation frequency and its light-induced modulation, we have created the equivalent circuit model of the device in LTspice,[35,36] which is illustrated in **Figure 2**a. In this model, constant current source I_d is the drive current used in the experiment. R_V is a voltage-controlled resistor representing the resistance of the VO_2 film, C_1 refers to the capacitance in the system that is connected in parallel to the VO_2 film. It should be noted that while I_d and C_1 are among the external components utilized in the experiment. Additional circuit elements including a voltage comparator (V_3), constant voltage sources (V_{b1}, V_{b2}, V_0), a constant resistor (R_0) and a capacitor (C_0) shown with a gray background, along with R_V are incorporated to imitate the variation of the PCM's voltage-controlled resistance (R_V) during phase transition. Details of the simulation are included in the Experimental section. Figure 2b plots the oscillation frequency of the circuit as a function of drive current during the dark conditions (blue) and when illuminated with an 8.7 μm wavelength IR laser(red). An increase in the oscillation frequency is observed during the light illumination compared to the dark condition. The simulation agrees well with the experimental results. It should be noted that the circuit can support oscillations in a certain range of the drive current. For the devices with $8 \times 8\ \mu m^2$ active area, oscillation onsets from the drive

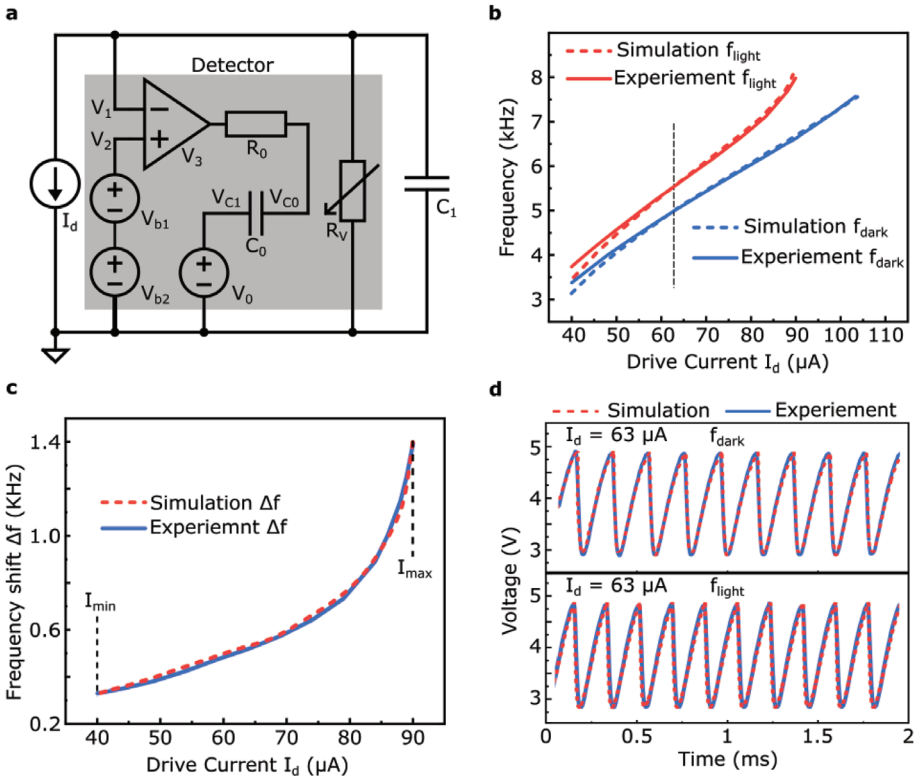

Figure 2. FM-based detector equivalent circuit model. a) Equivalent circuit diagram of the FM-based detector in LTspice. b) Evolution of the frequency of oscillation as a function of drive current I_d for an 8 × 8 μm^2 active detector area under dark (Blue) and light (Red) conditions. c) Simulated and experimental frequency shift Δf between light and dark conditions as a function of the drive current of the oscillator. d) Simulated and experimental waveform of the oscillator for a constant drive current of 63 μA during light and dark conditions.

current at 40 μA and ceases at 108 μA in the dark condition. When the drive current is lower than 40 μA, the voltage $V_1 < V_{th1}$ on the VO_2 film stays below the IMT threshold and consequently, no current oscillation exists. On the other hand, with a high drive current above 108 μA, the device makes an IMT but fails to make an MIT afterward due to $V_1 > V_{th2}$ at all the time, and hence the oscillation cannot exist as well. Here, I_{min} and I_{max} are referred to as the minimum and maximum limit currents that support oscillation in the circuit, respectively. The shift in the frequency in the presence of light ($\Delta f = f_{light} - f_{dark}$) as a function of drive current for a constant illumination power is shown in Figure 2c. It is observed that Δf increases with the drive current I_d. As the drive current I_d approaches the threshold current $I_{th2,}$ the increase in Δf is particularly rapid. Figure 2d displays the corresponding simulated (red dashed line) and experimental (blue solid line) oscillation waveforms at 63 μA in the dark (top) and the light (bottom) conditions. The experiments demonstrate that the frequency of the circuit increases from 5.007 kHz to 5.506 kHz when exposed to light, manifesting a frequency shift of Δf ~ 500 Hz which shows an excellent match with the simulation results.

2.3. Photoresponse with FM Detection Scheme

Next, the performance of the detector is assessed in terms of pixel dimensions. For this study, we characterized detectors of three different active areas: 8 × 8, 12 × 12, and 15 × 15 μm^2. **Figure 3**a shows the evolution of the oscillation frequency as a function of drive current for 3 different pixel sizes in dark and light conditions. The devices which are smaller in size (8 × 8 μm^2) exhibit the highest oscillation frequency with the same drive current. It is observed that both the limit current I_{min} and I_{max} are larger for the devices with 15 × 15 μm^2 pixel size. Despite the larger operation current, the bigger devices show lower frequency response under the same incident power compared to the smaller devices. The effect of pixel size on the behavior of the devices is attributed to the current density being lower in bigger pixels under the same drive current. The lower current density in the larger pixel leads to less local Joule heating, and hence higher drive currents are required to induce the phase transition in the larger pixels. Consequently, higher limit currents I_{min} and I_{max} are observed in the case of larger pixels. The decrease in the oscillation frequency with the bigger pixels can be explained by the longer time required to travel between two threshold voltages V_{th1} and V_{th2}, due to the larger difference between them $\Delta V = V_{th1} - V_{th2}$, further details can be found in Figure S2 (Supporting Information). Figure 3b shows the corresponding frequency shifts of 3 different pixel-size detectors. While the device with the dimension of 8 × 8 μm^2 exhibits the largest frequency shift, all 3 sizes show a similar trend as a function of drive current. From the frequency shift, the responsivity $\mathcal{R}$ can be determined as follows:

$$\mathcal{R} = \Delta f / P_{inc} \quad (1)$$

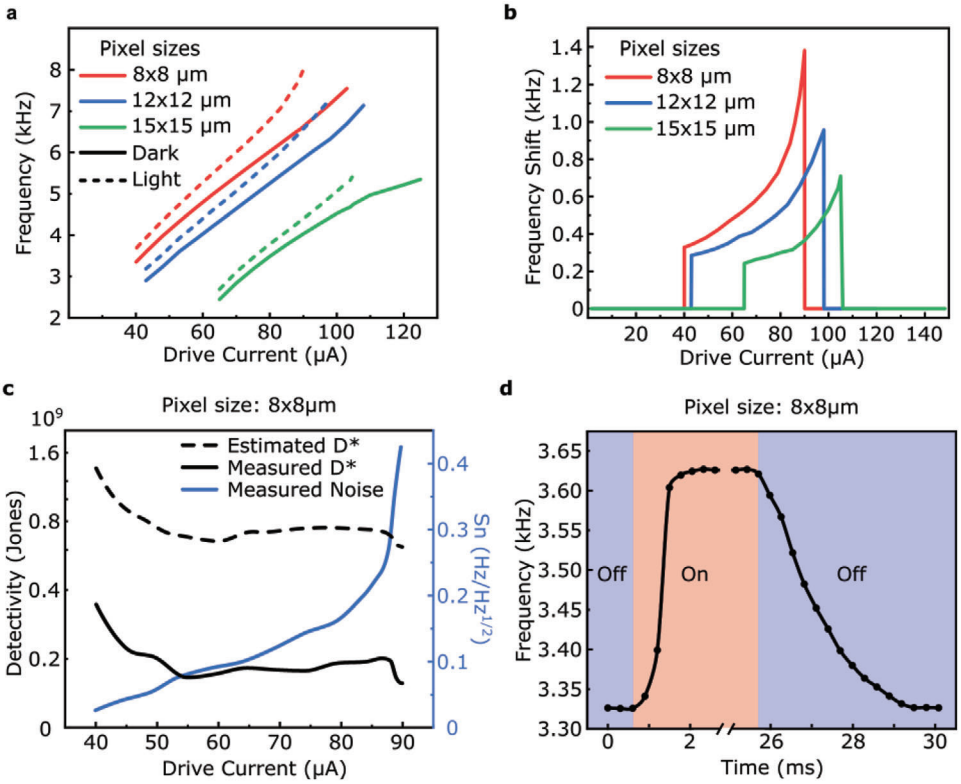

Figure 3. Detector LWIR performance measurements at room temperature. a) Evolution of oscillation frequency of the detector with respect to the driving current for three different sizes of the VO_2 channel, the corresponding frequency shift as a function of drive current is shown in b). The shift is presented as 0 when the circuit is not oscillating. c) Dependence of detectivity and noise of the detector on the drive current for an 8×8 μm^2 pixel. d) Measured time response of the 8×8 μm^2 device with the light switched on(red) and off(blue).

where P_{inc} is the incident power on the active region of the device. It is to be noted that since the spot diameter of the laser is ≈300 μm, P_{inc} is only a fraction of the total incident power. Therefore, from these measurements, it can be inferred that better responsivity is expected for devices with smaller pixel sizes. Further, the sensitivity of the device with 8×8 μm^2 active pixel area is assessed by measuring the detectivity (D^*) as a function of drive current. The D^* is defined by the expression

$$D^* = \sqrt{A}/NEP \tag{2}$$

where, A is the active area of the detector and NEP is the noise equivalent power. NEP can be determined by:

$$\mathrm{NEP} = S_n/\mathcal{R} \tag{3}$$

where S_n is the noise spectral density calculated at 1 Hz by a waveform measurement with Shannon-Nyquist sampling theorem. The noise is attributed to circuit FM noises such as phase noise and jitter noise.[37,38] The evolution of the noise and detectivity as a function of the drive current is plotted in Figure 3c. As the drive current increases, the noise (S_n) also increases because the device approaches the metallic phase. This is attributed to the increased instability of V_{th1} and V_{th1}-V_{th2} with a high drive current. The black graph in Figure 3c displays the measured D* of the device as a function of the drive current. This measurement demonstrates that when the drive current is set to the smallest value of 40 μA, producing the lowest noise S_n, the highest measured D* of 3.8×10^8 Jones is obtained for these fabricated detectors. As the drive current increases, the value of S_n also increases, leading to a corresponding decrease in D*. This decrease in D* continues until a certain drive current is attained, after which it remains mostly constant. The capacitance of the measurement setup is estimated to be ≈6 nF by matching experimental result with the equivalent circuit model prediction. It is worth noting that if the capacitance in parallel with the VO_2 film is reduced or the electrical circuit's instability is decreased, the sensitivity of the proposed FM-based detector for room temperature use will be further enhanced. According to industry standards, constructing a measurement set-up with a parallel capacitance of 1 nF is a straightforward task. Therefore, the D* of the device with 1 nF capacitance is predicted by the equivalent circuit and represented by the red curve in Figure 3d, demonstrating a four-fold improvement in the D* value is achievable. For a drive current of 40 μA, it is anticipated that the highest expected D* is $\approx 1.5 \times 10^9$ Jones with room temperature detection, which is a level achievable only with a cryogenically cooled LWIR detector among commercially available detectors. The time response is then studied as shown in Figure 3d. The light source is turned on/off with the on/off of the control current of the QCL. The calculated response time τ_{total} is ≈2.96 ms at 40 μA by the rise time τ_{rise} and fall time τ_{fall} by $\tau_{total} = \tau_{rise} + \tau_{fall}$. τ_{rise}/τ_{fall} is calculated by the duration

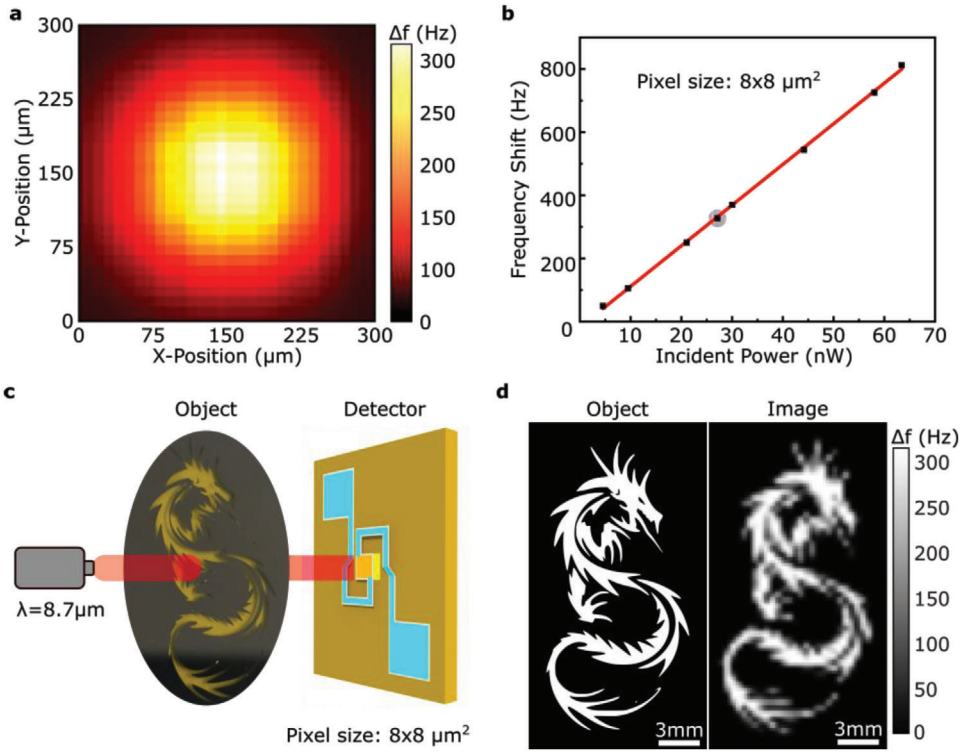

Figure 4. FM based infrared imaging. a) Frequency shift map of the laser beam profile obtained by scanning an 8 × 8 μm² size pixel. b) Dependence of the Frequency shift on the incident power showing a linear detector response. c) Schematic illustration of the experimental setup of the single-pixel imaging system. The light source and detector are fixed while the object is mounted on the motorized XY-stage for scanning. d) Original design of the object (left) and the obtained image (right) through single-pixel imaging in terms of frequency shift.

between 10% and 90% of changes in steady-state frequencies.[39] The result is 5–7 times faster compared to the commercially available uncooled LWIR detectors in the market.[7,40,41] The short response time of the proposed detector can be attributed to the strong electrothermal feedback in VO_2 thin film.[42,43]

Next, the dependency of the frequency response of the device to the incident IR power is investigated. As discussed previously, the spot size of the excitation laser, with a wavelength of 8.7 μm, is much larger than the active area of the detector, which is 8 × 8 μm². Therefore, an accurate estimation of the incident power on the active area of the detector is necessary. For this purpose, we obtain the beam profile of the incident laser in the form of a frequency shift map by scanning the detector within the focal plane of the incident laser. The parabolic mirror used to focus the laser is shifted in increments of 10 μm with a motorized XY stage in order to scan the detector within the laser spot. **Figure 4**a is the measured frequency shift map of the perfectly Gaussian beam profile of the incident laser. The incident power P_{inc} on the active area of the detector is finally calculated by picking out the center 8 × 8 μm² region of the measured frequency shift map as:

$$P_{inc} = \left(\Delta f_d / \Delta f_{map}\right) \times P_{map} \quad (4)$$

where Δf_d is the integrated frequency shift over the center 8 × 8 μm² region of the map; Δf_{map} is the integrated frequency shift of the whole map; and P_{map} is the total incident power which is measured in front of the parabolic mirror by a power meter. The same measurements are performed to determine the incident laser power for the estimation of $\mathcal{R}$, NEP, and D*. Figure 4b shows the shift in oscillation frequency Δf as a function of incident laser power for an 8 × 8 μm² device. The power of the laser is varied using neutral density filters before the parabolic mirror. A linear response is observed for a large range of incident power on the 8 × 8 μm² area from 4.54 to 63.4 nW. The device position relative to the beam is carefully adjusted and placed at the center of the beam by scanning the beam profile for each incident power at the start of the measurement. To demonstrate the performance of our LWIR detector, a single-pixel imaging experiment was conducted. The setup for the experiment is illustrated in Figure 4c. The QCL laser is sent through a hollow mask of a dragon onto the detector. By changing the position of the mask, we were able to produce the image of the dragon as shown in Figure 4d. It is to be noted that the captured image is a map of frequency shift as opposed to amplitude shift in conventional imaging techniques. Sharp high-resolution features are clearly visible in the captured image. We believe this is the first demonstration of FM-based LWIR imaging.

3. Conclusion

In summary, we have demonstrated an FM-based uncooled LWIR detector using a cavity-coupled PCM. The FM-based detection scheme possesses inherent robustness against noise compared to conventional AM-based detection schemes, providing

significant improvement in sensitivity and signal-to-noise ratio while minimizing the influence of external interference. The measured detectivity of the proposed detector is higher than commercially available uncooled LWIR detectors with a faster response time. We expect that a proper industrial packaging with low capacitance circuit components can further increase the detectivity comparable to cryogenically cooled detectors ($\approx 10^9$). Notably, the detector exhibits a highly desirable linear response and high detectivity at room temperature, rendering it a promising solution for diverse applications. Furthermore, we have demonstrated the feasibility of developing a multipixel IR camera with these detectors through single-pixel imaging. Although, we employed VO_2 as the phase change material in our work, this detection scheme can be extended to other PCM exhibiting NDR, and different spectral regions of light can be covered depending on the absorption properties of the material. Furthermore, PCMs such as W-doped VO_2 with lower phase transition temperature[44] can be operated with smaller drive current, which is beneficial for a dense focal plane array formation. The operational wavelength may also be tuned by changing the cavity thickness. Our results introduce this novel FM-based detector as a unique platform for creating low-cost, high-efficiency uncooled infrared detectors and imaging systems for various applications such as remote sensing, thermal imaging, and medical diagnostics.

4. Experimental Section

Fabrication: A 120 nm thick Au mirror was fabricated on SiO_2(300 nm)/Si(500 µm) substrate by UV-photolithography and e-beam metal deposition. Polyimide was then patterned with UV-photolithography assisted by a photoresist mask and finally cured at 350 °C under vacuum for 5 h. Two hundred nanometers Si_3N_4 was deposited on the sample by plasma-enhanced chemical vapor deposition (PECVD). The supporting structure was then patterned out of the Si_3N_4 by UV-photolithography and reactive ion etching (RIE) with CF_4. Next, an 150 nm VO_2 film was deposited on the Si_3N_4 structure through magnetron sputtering. Electrodes were then patterned by UV-photolithography 60 nm chromium deposition. Finally, the VO_2 film was patterned into microfilms by UV-photolithography, followed by RIE with SF_6.

Measurement: *Electrical Measurements*: The fabricated device was driven by a constant current source with a source measurement unit (Keithley 2614B). No capacitor was attached but the total capacitance (6 nF) of the system was extracted by fitting the experimental data with the simulation. The device was mounted on a probe station (MPI TS150). The oscillation waveform of the voltage across the VO_2 film was recorded by a digital storage oscilloscope (Tektronix Mix Domain Oscilloscope MDO34).

Optical Setup: A quantum cascade laser source (OmniLux from Pranalytica, Inc.) at 8.7 µm was focused by a parabolic mirror onto the VO_2 film. Laser power at different positions in the beam path was measured by a power meter (Thermal Power Sensor S401C from Thorlabs). Neutral density filters (Thorlabs) were used to scale the incident power. For mapping the beam profile, the parabolic mirror was moved by a motorized XY-stage (M30X, Thorlabs), while the device was kept static. For the single-pixel imaging experiment, a chromium mask on top of ZnSe window (WG70530 from Thorlabs) was placed in between the parabolic mirror and the device. The diameter of the mask plate (ZnSe window) was 2.54 cm, while the size of the dragon pattern on top was 1 to 2.1 cm. The laser was focused on the mask to achieve the best resolution of the recorded image. Both the parabolic mirror and the sample were kept static, while the mask was moved by the motorized XY-stage (M30X, Thorlabs).

FDTD Simulation: Simulation for absorption was performed in Lumerical FDTD. The refractive index values for VO_2 were extracted by ellipsometry measurement (VASE Ellipsometer, J.A. Woollam).

LTSpice Simulation: The equivalent circuit modeling of the VO_2 detector was done in LTSpice. The schematic illustration of the equivalent circuit is shown in Figure 2a. I_d represents the drive current of the circuit from the constant current source used in the experiment. R_V was a resistor signifying the resistance of the VO_2 film. C_1 was the total capacitance in the system which is in parallel to the VO_2 film. Although I_d, R_V, and C_1 were all the components that are present in the experiment, more circuit components were added to mimic the current/voltage-controlled variation of the resistance R_V of the VO_2 film. Three major components: a voltage comparator V_3, a capacitor C_0, and a constant voltage source $V_0 = 1$ V were added along with some other components, whose values were tuned to best match the experimental results. These components include a voltage source $V_{b1} = F(V_{th1}, V_{light}, Id) - \alpha V_{th2}$, a constant voltage source $V_{b2} = V_{th2}$, and a constant resistance R_0. The resistance change between the insulating and the metallic phase of the VO_2 film was incorporated by making R_V a voltage-controlled resistor

$R_V = 1/ (V_{C0}{*}G_{ins} + (V_{C1} - V_{C0}){*}G_{met})$, where G_{ins} and G_{met} are the conductance of VO_2 film in its insulating phase and metallic phase respectively. The equivalent circuit incorporates the MIT and IMT of the VO_2 film in the simulation in the following manner: When the VO_2 film is in its insulating phase, the voltage across the VO_2 film is low (terminal V1 of the comparator), the voltage comparator V_3 outputs $V_{C0} = 1$ V. Therefore, the voltage-controlled resistance is calculated following the equation Rv = 1/Gins, which matches with the insulating phase. Similarly, in the metallic phase of VO_2, the voltage comparator outputs 0 V making $R_V = 1/G_{met}$. The capacitor C_0 stores the information of the phase status of the VO_2 film with the voltage difference between the 2 sides V_{C1}-V_{C0}.

Supporting Information

Supporting Information is available from the Wiley Online Library or from the author.

Acknowledgements

This work at University of Central Florida was partially supported by National Science Foundation Grant #ECCS-2015722 and Samsung Global Research Outreach Award 2022.

Conflict of Interest

The authors declare no conflict of interest.

Data Availability Statement

The data that support the findings of this study are available from the corresponding author upon reasonable request.

Keywords

frequency modulation, Infrared detection, phase change materials, uncooled detectors

Received: August 7, 2023
Revised: September 28, 2023
Published online:

[1] J. Liu, F. Xia, D. Xiao, F. J. García De Abajo, D. Sun, *Nat. Mater.* **2020**, *19*, 830.

[2] J. J. Talghader, A. S. Gawarikar, R. P. Shea, *Light: Sci. Appl.* **2012**, *1*, 24.
[3] B. Ferguson, X.-C. Zhang, *Nat. Mater.* **2002**, *1*, 26.
[4] C. L. Tan, H. Mohseni, *Nanophotonics* **2018**, *7*, 169.
[5] W. Lei, J. Antoszewski, L. Faraone, *Appl. Phys. Rev.* **2015**, *2*, 041303.
[6] A. Rogalski, *Rep. Prog. Phys.* **2005**, *68*, 2267.
[7] P. L. Richards, *J. Appl. Phys.* **1994**, *76*, 1.
[8] P. V. K. Yadav, I. Yadav, B. Ajitha, A. Rajasekar, S. Gupta, Y. Ashok Kumar Reddy, *Sens. Actuators, A* **2022**, *342*, 113611.
[9] S. Donati, *Photodetectors: devices, circuits and applications*, John Wiley & Sons, Hoboken, NJ **2021**.
[10] J. D. Vincent, S. Hodges, J. Vampola, M. Stegall, G. Pierce, *Fundamentals of Infrared and Visible Detector Operation and Testing*, John Wiley & Sons, Hoboken, NJ **2015**.
[11] Y. Ke, S. Wang, G. Liu, M. Li, T. J. White, Y. Long, *Small* **2018**, *14*, 1802025.
[12] J. Goodenough, *Prog. Solid State Chem.* **1971**, *5*, 145.
[13] J. Q. Shen, *Ann. Phys.* **2004**, *13*, 532.
[14] T. Sasaki, H. Ueda, T. Kanki, H. Tanaka, *Sci. Rep.* **2015**, *5*, 17080.
[15] K. Liu, S. Lee, S. Yang, O. Delaire, J. Wu, *Mater. Today* **2018**, *21*, 875.
[16] Z. Shao, X. Cao, H. Luo, P. Jin, *NPG Asia Mater* **2018**, *10*, 581.
[17] M.-J. Lee, Y. Park, D.-S. Suh, E.-H. Lee, S. Seo, D.-C. Kim, R. Jung, B.-S. Kang, S.-E. Ahn, C. B. Lee, D. H. Seo, Y.-K. Cha, I.-K. Yoo, J.-S. Kim, B. H. Park, *Adv. Mater.* **2007**, *19*, 3919.
[18] A. Crunteanu, J. Givernaud, J. Leroy, D. Mardivirin, C. Champeaux, J.-C. Orlianges, A. Catherinot, P. Blondy, *Sci. Technol. Adv. Mater.* **2010**, *11*, 065002.
[19] X. Xu, X. He, H. Wang, Q. Gu, S. Shi, H. Xing, C. Wang, J. Zhang, X. Chen, J. Chu, *Appl. Surf. Sci.* **2012**, *261*, 83.
[20] S. K. Nandi, S. K. Das, C. Estherby, A. Gentle, R. G. Elliman, *J. Appl. Phys.* **2020**, *128*, 244103.
[21] E. Corti, B. Gotsmann, K. Moselund, A. M. Ionescu, J. Robertson, S. Karg, *Solid-State Electron.* **2020**, *168*, 107729.
[22] N. Shukla, A. Parihar, E. Freeman, H. Paik, G. Stone, V. Narayanan, H. Wen, Z. Cai, V. Gopalan, R. Engel-Herbert, D. G. Schlom, A. Raychowdhury, S. Datta, *Sci. Rep.* **2014**, *4*, 4964.
[23] G. Karaoglan-Bebek, M. N. F. Hoque, M. Holtz, Z. Fan, A. A. Bernussi, *Appl. Phys. Lett.* **2014**, *105*, 201902.
[24] A. Parihar, N. Shukla, M. Jerry, S. Datta, A. Raychowdhury, *Nanophotonics* **2017**, *6*, 601.
[25] S. Dutta, A. Parihar, A. Khanna, J. Gomez, W. Chakraborty, M. Jerry, B. Grisafe, A. Raychowdhury, S. Datta, *Nat. Commun.* **2019**, *10*, 3299.
[26] M. Salverda, R. P. Hamming-Green, B. Noheda, *J. Phys. D: Appl. Phys.* **2022**, *55*, 335305.
[27] X. Liu, S. Li, S. K. Nandi, D. K. Venkatachalam, R. G. Elliman, *J. Appl. Phys.* **2016**, *120*, 124102.
[28] S. K. Das, S. K. Nandi, C. V. Marquez, A. Rúa, M. Uenuma, E. Puyoo, S. K. Nath, D. Albertini, N. Baboux, T. Lu, Y. Liu, T. Haeger, R. Heiderhoff, T. Riedl, T. Ratcliff, R. G. Elliman, *Adv. Mater.* **2023**, *35*, 2208477.
[29] C. Zhu, Y. Chen, F. Liu, S. Zheng, X. Li, A. Chaturvedi, J. Zhou, Q. Fu, Y. He, Q. Zeng, H. J. Fan, H. Zhang, W.-J. Liu, T. Yu, Z. Liu, *ACS Nano* **2018**, *12*, 11203.
[30] A. Safaei, S. Chandra, A. Vázquez-Guardado, J. Calderon, D. Franklin, L. Tetard, L. Zhai, M. N. Leuenberger, D. Chanda, *Phys. Rev. B* **2017**, *96*, 165431.
[31] M. Pattanayak, M. N. F. Hoque, Z. Fan, A. A. Bernussi, *Sci. Technol. Adv.* **2018**, *19*, 693.
[32] A. Zimmers, L. Aigouy, M. Mortier, A. Sharoni, S. Wang, K. G. West, J. G. Ramirez, I. K. Schuller, *Phys. Rev. Lett.* **2013**, *110*, 056601.
[33] H.-T. Kim, B.-G. Chae, D.-H. Youn, G. Kim, K.-Y. Kang, S.-J. Lee, K. Kim, Y.-S. Lim, *Appl. Phys. Lett.* **2005**, *86*, 242101.
[34] T. Oka, R. Arita, H. Aoki, *Phys. Rev. Lett.* **2003**, *91*, 066406.
[35] P. Maffezzoni, L. Daniel, N. Shukla, S. Datta, A. Raychowdhury, *IEEE Trans. Circuits Syst. I* **2015**, *62*, 2207.
[36] S. Amer, M. S. Hasan, M. M. Adnan, G. S. Rose, *IEEE TCAS-I* **2019**, *7*, 18.
[37] A. Hajimiri, S. Limotyrakis, T. H. Lee, *IEEE J. Solid-State Circuits* **1999**, *34*, 790.
[38] M. Lax, *Phys. Rev.* **1967**, *160*, 290.
[39] M. Zhang, F. Zhang, Y. Wang, L. Zhu, Y. Hu, Z. Lou, Y. Hou, F. Teng, *Sci. Rep.* **2018**, *8*, 11157.
[40] C. Li, *Opt. Eng.* **2011**, *50*, 061017.
[41] T. Schimert, C. Hanson, J. Brady, T. Fagan, M. Taylor, W. McCardel, R. Gooch, M. Gohlke, A. Syllaios, presented at *Infrared Technology and Applications XXXV*, Orlando, Florida, May **2009**.
[42] G. Neto, *Opt. Eng.* **2008**, *47*, 073603.
[43] K. D. Irwin, *Appl. Phys. Lett.* **1995**, *66*, 1998.
[44] K. Sun, C. Wheeler, J. A. Hillier, S. Ye, I. Zeimpekis, A. Urbani, N. Kalfagiannis, O. L. Muskens, C. H. (K.) De Groot, *Adv. Opt. Mater.* **2022**, *10*, 2201326.